JOURNAL OF COMPUTATIONAL PHYSICS 29, 101–126 (1978)

Dynamical Grid Method for Time-Dependent Simulations of Axisymmetric Instabilities in Tokamaks*

S. C. JARDIN, J. L. JOHNSON,† J. M. GREENE, AND R. C. GRIMM

Plasma Physics Laboratory, Princeton University, Princeton, New Jersey 08540

Received July 6, 1977; revised November 3, 1977

A natural nonorthogonal time-dependent coordinate transformation based on the magnetic field lines is utilized for the numerical integration of the two-dimensional axisymmetric time-dependent ideal MHD equations in tokamak geometry. The finite-difference grid is treated as a dynamical variable, and its equations of motion are integrated simultaneously with those for the fluid and magnetic field. The method is applicable to tokamak systems of arbitrary pressure and cross section. It is particularly useful for the nearly incompressible ideal MHD modes which are of interest in tokamak stability studies.

1. INTRODUCTION

The numerical solution of the time-dependent equations of magnetohydrodynamics (MHD) promises to provide an exceedingly useful tool for both the theorist and the experimentalist engaged in plasma physics and controlled thermonuclear fusion research. Appropriate simulations help to bridge the gap between theoretical and experimental results. Complex geometries, nonlinear effects, and realistic boundary conditions can only be treated adequately numerically. Physical effects can be isolated and analytic approximations can be suggested or tested.

Numerical methods for calculating the nonlinear transient dynamics of multidimensional ideal MHD stability phenomena in tokamaks have recently begun to appear in the literature. The primary difficulty to be overcome lies in the multiplicity of time scales associated with the linear MHD spectrum [1]. For a system with field strength B_0, minor radius a, and density ρ_0, a discrete set of fast compressible modes are present with characteristic times

$$\omega_f^{-1} \sim a(\rho_0)^{1/2}/B_0 .$$

This motion is much faster than the nearly incompressible transverse modes, associated with MHD stability phenomena, which have characteristic times

$$\omega_T^{-1} \sim \left(\frac{a(\rho_0)^{1/2}}{B_0}\right)\left(\frac{Rq}{a}\right),$$

* Supported by U. S. ERDA Contract EY-76-C-02-3073.

† On loan from Westinghouse Research and Development Center, Pittsburgh, Pa.

0021-9991/78/0291-0101$02.00/0

where R is the major radius and q is the safety factor at the limiter. The factor Rq/a is typically 10 to 30 in tokamaks of interest.

Previous methods have dealt with this disparity in one of two ways. One [2–4] is to use the limiting form of the MHD equations as $Rq/a \to \infty$. This forces incompressibility and thus annihilates the fast waves altogether, leaving only the transverse time scale in the equations. The other [5–8] approach has been to integrate the primitive compressible equations without taking special care to isolate phenomena occurring on different time scales. This approach is useful when simulating tokamaks with small Rq/a and large $\beta \sim 2p/B^2$ so that the transverse and the fast time scales come together.

We describe here the dynamical grid method [9], a new technique for solving the MHD equations in axisymmetric tokamak geometry. It is neither Eulerian nor Lagrangian, but is based on the structure of the changing magnetic field. This method is particularly useful for studying tokamak parameters of arbitrarily low β and large aspect ratio where a distinct time scale separation occurs. Instead of annihilating the compressible fast time scale phenomena analytically, we average over it numerically by using a partially implicit method. This is made possible by introducing a time-dependent nonorthogonal magnetic flux coordinate transformation that determines the grid used in the computation.

The positions of the grid points are treated as dynamical variables. The time-advancement equations for these are integrated simultaneously with the conservation equations for the fluid and the magnetic field. The equations of motion of the grid

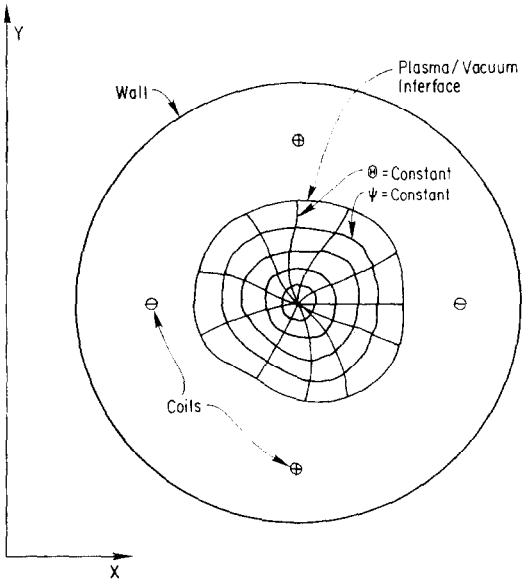

FIG. 1. Plasma with arbitrary shape and conducting wall. In cylindrical geometry, this is the cross section of a cylinder. In toroidal geometry, it is the cross section of a torus.

are chosen for convenience. The coordinate system conforms to the fluid in such a way that the characteristics of the partial differential equations can be represented accurately, but there is also some slippage of the fluid with respect to the grid so that wave phenomena occurring on different time scales can be approximately isolated.

We solve a free-boundary problem with both a plasma and a vacuum region (Fig. 1). The plasma–vacuum interface is represented accurately and the elliptic field equations in the vacuum are solved by utilizing a Green's function technique.

In Section 2 we discuss the coordinate system utilized in the plasma region and describe how the velocity of a fluid element is divided into the local velocity of the coordinate system and a velocity relative to that moving system. We recast the MHD equations for the plasma and the vacuum in this coordinate system in Sections 3 and 4. In Section 5 we present the finite-difference method used to solve these equations. In the remainder of the text, we present examples which illustrate the accuracy and the applicability of the dynamical grid method. For clarity, the discussion in the text is limited to cylindrical symmetry. In the appendix we give the appropriate generalizations to toroidal geometry.

2. A Convenient Coordinate System

The success of the dynamical grid method is due largely to the selection of appropriate coordinates. We define a coordinate system (ψ, Θ, ϕ) with the following properties:

(a) ψ is a magnetic surface label proportional to the area inside a magnetic surface, normalized to π at the plasma boundary.

(b) Θ is a periodic coordinate $0 \leqslant \Theta \leqslant 2\pi$. The $\Theta = 0$ ray is a straight line; i.e., $\partial y/\partial \psi \,|_{\Theta=0} = 0$.

(c) ϕ is the ignorable coordinate (i.e., $\partial/\partial\phi \equiv 0$), normalized such that $|\, \nabla\phi \,|^2 = k^2$.

(d) The Jacobian is everywhere equal to a constant

$$\mathscr{J}^{-1} \equiv \nabla\psi \times \nabla\Theta \cdot \nabla\phi = 2\pi k\, T(t),$$

where π/T is the area of the plasma column.

(e) $\nabla\Theta$ and $\nabla\psi$ are both orthogonal to $\nabla\phi$ but are not orthogonal to each other.

Here $k = 2\pi/L$ is a constant in cylindrical geometry and is the reciprocal major radius in the toroidal generalization given in the appendix. These conditions completely determine the coordinate system.

The use of the surface label ψ as a coordinate is desirable for several reasons. One is that it enables the avoidance of "numerical resistivity" and thus erroneous magnetic field line diffusion due to numerical truncation errors. Another is that since two of the three wave solutions allowed by the tokamak-ordered MHD equations propagate

along **B**, the use of ψ is essential for separating phenomena occurring on different time scales. A third reason is to make possible the accurate calculation of interface dynamics at the plasma–vacuum boundary.

The physical interpretation of the surface label ψ and the complete definition of the angle variable Θ are given by specification (d) that the Jacobian be independent of ψ and Θ and depend only on the time t. This form for the Jacobian is desirable since it implies that the area of each computational zone remains the same. Prescribing the Jacobian to be of this form enables lowest-order isolation of phenomena occurring on the fast and the transverse time scales.

The (ψ, Θ, ϕ) coordinate system is nonorthogonal since $\nabla\Theta \cdot \nabla\psi \neq 0$. The coordinate transformation which relates this to a Cartesian system is time dependent since the magnetic surfaces move. Indeed, solving for this coordinate transformation is a major part of the solution procedure.

We treat (ψ, Θ, ϕ) as independent variables and the Cartesian coordinates x and y as dependent variables. Subscripts denote differentiation in the (ψ, Θ, ϕ) coordinate system. The following relations then hold:

Jacobian:

$$\mathcal{J} = \frac{1}{k}(x_\psi y_\Theta - y_\psi x_\Theta);$$

Metric tensor:

$$g^{11} \equiv |\nabla\psi|^2 = \frac{1}{(\mathcal{J}k)^2}(x_\Theta^2 + y_\Theta^2),$$

$$g^{22} \equiv |\nabla\Theta|^2 = \frac{1}{(\mathcal{J}k)^2}(x_\psi^2 + y_\psi^2),$$

$$g^{12} \equiv g^{21} \equiv \nabla\Theta \cdot \nabla\psi = \frac{-1}{(\mathcal{J}k)^2}(x_\Theta x_\psi + y_\Theta y_\psi),$$

$$g^{33} \equiv |\nabla\phi|^2 = k^2;$$

Christoffel symbols:

$$\begin{Bmatrix} 1 \\ 1\ 1 \end{Bmatrix} = \frac{1}{k\mathcal{J}}(y_\Theta x_{\psi\psi} - x_\Theta y_{\psi\psi}), \qquad \begin{Bmatrix} 1 \\ 2\ 2 \end{Bmatrix} = \frac{1}{k\mathcal{J}}(y_\Theta x_{\Theta\Theta} - x_\Theta y_{\Theta\Theta}),$$

$$\begin{Bmatrix} 2 \\ 1\ 1 \end{Bmatrix} = \frac{1}{k\mathcal{J}}(x_\psi y_{\psi\psi} - y_\psi x_{\psi\psi}), \qquad \begin{Bmatrix} 2 \\ 2\ 2 \end{Bmatrix} = \frac{1}{k\mathcal{J}}(x_\psi y_{\Theta\Theta} - y_\psi x_{\Theta\Theta}).$$

$$\begin{Bmatrix} 1 \\ 2\ 1 \end{Bmatrix} = \begin{Bmatrix} 1 \\ 1\ 2 \end{Bmatrix} = \frac{1}{k\mathcal{J}}(y_\theta x_{\psi\Theta} - x_\theta y_{\psi\Theta}),$$

$$\begin{Bmatrix} 2 \\ 2\ 1 \end{Bmatrix} = \begin{Bmatrix} 2 \\ 1\ 2 \end{Bmatrix} = \frac{1}{k\mathcal{J}}(x_\psi y_{\psi\Theta} - y_\psi x_{\psi\Theta}).$$

Using these coordinates, the magnetic field can be expressed in terms of two scalar functions $f(\psi, t)$ and $g(\psi, \Theta, t)$;

$$\mathbf{B} = B_0[f(\psi, t)\,\nabla\phi \times \nabla\psi + (1/k)g(\psi, \Theta, t)\,\nabla\phi], \tag{1}$$

where B_0 is a constant. This is the most general axially symmetric solution of $\nabla \cdot \mathbf{B} = 0$ and $\mathbf{B} \cdot \nabla\psi = 0$. The normalization constants B_0 and k are chosen so that both f and g are of order unity. Since the plasma area has been normalized to π, this makes k the small parameter in the usual tokamak expansion.

Faraday's law and the condition that $\mathbf{B} \cdot \nabla\psi = 0$ relate the coordinate system to the fluid. They must move in harmony but are not frozen together. The coordinate slippage is determined by the requirement that the Jacobian remain constant in space. Thus, the absolute velocity of a fluid element divides naturally and uniquely into two parts;

$$\mathbf{v} = \mathbf{v}^L + \mathbf{v}^E,$$

where

$$\mathbf{v}^L \equiv x_t(\psi, \Theta, t)\hat{\mathbf{x}} + y_t(\psi, \Theta, t)\hat{\mathbf{y}}$$

is the Lagrangian velocity of the (ψ, Θ, ϕ) coordinate system and

$$\mathbf{v}^E \equiv u(\psi, \Theta, t)\mathcal{J}\nabla\Theta \times \nabla\phi + v(\psi, \Theta, t)\mathcal{J}\nabla\phi \times \nabla\psi + w(\psi, \Theta, t)\mathcal{J}\nabla\psi \times \nabla\Theta$$

is the Eulerian velocity of the fluid relative to the moving coordinate system. The Lagrangian velocity determines how the metric tensor changes in time. Also, since the computational grid lines are coordinate lines, they move with the Lagrangian velocity.

The requirement that $\mathcal{J}^{-1} = 2\pi kT(t)$ is equivalent to demanding that x and y satisfy the relation

$$(x_\psi y_\Theta - x_\Theta y_\psi) = 1/2\pi T(t). \tag{2}$$

This constraint can be satisfied for $T_t = 0$ by the introduction of a stream function $\xi(\psi, \Theta, t)$. When $T_t \neq 0$, the concept of a stream function must be generalized to allow for motions in which the entire coordinate system expands uniformly (isotropic expansion). If Eq. (2) is satisfied everywhere at time $t = 0$, it will always be satisfied everywhere provided x and y are advanced using

$$x_t = x_\psi \Lambda + x_\Theta \Omega, \tag{3}$$
$$y_t = y_\psi \Lambda + y_\Theta \Omega, \tag{4}$$

where

$$\Lambda \equiv T\xi_\Theta - \pi T_t\{[x - x(0)]\, y_\Theta - [y - y(0)]\, x_\Theta\}, \tag{5}$$
$$\Omega \equiv -T\xi_\psi + \pi T_t\{[x - x(0)]\, y_\psi - [y - y(0)]\, x_\psi\}, \tag{6}$$

and $[x(0), y(0)]$ are the coordinates of the magnetic axis.

3. Plasma Region Equations

The equations of ideal MHD are:

The equation of continuity

$$\frac{\partial \rho}{\partial t} + \nabla \cdot (\rho \mathbf{v}) = 0; \tag{7}$$

the equation of motion

$$\rho\left(\frac{\partial \mathbf{v}}{\partial t} + \mathbf{v}\cdot\nabla\mathbf{v}\right) = \mathbf{J}\times\mathbf{B} - \nabla p; \tag{8}$$

the equation of state

$$\frac{\partial}{\partial t} p^{1/\gamma} + \nabla\cdot(p^{1/\gamma}\mathbf{v}) = 0, \tag{9}$$

Maxwell's equations

$$\frac{\partial \mathbf{B}}{\partial t} = -\nabla\times\mathbf{E}, \tag{10}$$

$$\nabla\cdot\mathbf{B} = 0, \tag{11}$$

$$\mathbf{J} = \nabla\times\mathbf{B}; \tag{12}$$

and the infinite-conductivity Ohm's law

$$\mathbf{E} + \mathbf{v}\times\mathbf{B} = 0. \tag{13}$$

Equations (7) and (9) imply the condition $d(p\rho^{-\gamma})/dt = 0$ that the entropy of each fluid element is conserved. In our coordinate system, these equations can be cast as

$$\bar{\rho}_t + (\bar{\rho}u)_\psi + (\bar{\rho}v)_\Theta = 0, \tag{14}$$

$$f_t + (fu)_\psi = 0, \tag{15}$$

$$\bar{g}_t + (\bar{g}u)_\psi + (\bar{g}v - 2\pi f w)_\Theta = 0, \tag{16}$$

$$u_\Theta = 0, \tag{17}$$

$$\bar{p}_t + (\bar{p}u)_\psi + (\bar{p}v)_\Theta = 0, \tag{18}$$

$$(u+\Lambda)_t + \frac{1}{\rho}|\nabla\psi|^2 P_\psi + \frac{1}{\rho}\nabla\Theta\cdot\nabla\psi\, P_\Theta + R = 0, \tag{19}$$

$$(v+\Omega)_t + \frac{1}{\rho}\nabla\Theta\cdot\nabla\psi\, P_\psi + \frac{1}{\rho}|\nabla\Theta|^2 P_\Theta + S = 0, \tag{20}$$

$$(w\bar{\rho})_t + (\bar{\rho}vw)_\Theta + (\bar{\rho}uw)_\psi - 2\pi B_0^2 f g_\Theta k^2 = 0. \tag{21}$$

Here

$$\bar{\rho} \equiv \rho/T,$$

$$\bar{g} \equiv g/T,$$

$$\bar{p} \equiv p^{1/\gamma}/T,$$

$$P \equiv \tfrac{1}{2}B^2 + p,$$

$$\begin{aligned} R \equiv{}& v(u+\Lambda)_\Theta + u(u+\Lambda)_\psi + (u+\Lambda)\Lambda_\psi + (v+\Omega)\Lambda_\Theta + (u+\Lambda)^2\begin{Bmatrix}1\\1\ 1\end{Bmatrix} \\ &+ (v+\Omega)^2\begin{Bmatrix}1\\2\ 2\end{Bmatrix} + 2(u+\Lambda)(v+\Omega)\begin{Bmatrix}1\\2\ 1\end{Bmatrix} - (2\pi k B_0 f T)^2\begin{Bmatrix}1\\2\ 2\end{Bmatrix}/\rho, \\ S \equiv{}& v(v+\Omega)_\Theta + u(v+\Omega)_\psi + (u+\Lambda)\Omega_\psi + (v+\Omega)\Omega_\Theta + (u+\Lambda)^2\begin{Bmatrix}2\\1\ 1\end{Bmatrix} \\ &+ (v+\Omega)^2\begin{Bmatrix}2\\2\ 2\end{Bmatrix} + 2(u+\Lambda)(v+\Omega)\begin{Bmatrix}2\\1\ 2\end{Bmatrix} - (2\pi k B_0 f T)^2\begin{Bmatrix}2\\2\ 2\end{Bmatrix}/\rho. \end{aligned} \tag{22}$$

Equations (3) and (4), (14)–(16), and (18)–(21) provide 9 equations to advance the 11 time-dependent variables x, y, T, ξ, ρ, f, g, p, u, v, and w, supplemented by the contraint, Eq. (17), on u and

$$\xi(\psi, \Theta = 0, t) = -2\pi[\, y_t(0)]x(\psi, \Theta = 0, t), \tag{23}$$

$$u(\psi = \pi, t) = 0. \tag{24}$$

Then the five conditions on the coordinate system given in Section 2 are satisfied at all times.

Equation (19) determines the time advancement of the variable $U \equiv u + \Lambda$. To incorporate the constraints, Eqs. (17) and (24), we decompose U by averaging over a flux surface and using Eqs. (5) and (17) to obtain the identities

$$\langle U \rangle \equiv u - \pi T_t \langle x y_\Theta - y x_\Theta \rangle, \tag{25}$$

$$U - \langle U \rangle \equiv T\xi_\Theta - \pi T_t\{[x - x(0)]\, y_\Theta - [\, y - y(0)]\, x_\Theta - \langle x y_\Theta - y x_\Theta \rangle\}. \tag{26}$$

The first of these is evaluated at $\psi = \pi$ and used with Eq. (24) to determine $T_t(t)$. It determines $u(\psi, t)$ everywhere else. The second determines ξ_Θ everywhere, with ξ obtained by numerically integrating ξ_Θ on each flux surface using Eq. (23).

Initial conditions are necessary for each variable being integrated forward in time. The only spatial boundary of the plasma is the free boundary at the plasma–vacuum interface $\psi = \pi$. Boundary conditions are not necessary for ρ, f, g, and p since Eqs. (14)–(16) and (18) are in conservation form and $u = 0$ at $\psi = \pi$. This reflects the ideal MHD conservation of mass, poloidal and toroidal flux, and entropy. The motion of the plasma boundary is computed in the same way that the motion of an interior point is computed. This is made possible since the total pressure, $P \equiv p + \frac{1}{2}B^2$, is continuous across the plasma–vacuum interface and, therefore, can be differentiated there. The computation of P in the vacuum region is discussed in Section 4. The other physical boundary condition at the plasma–vacuum interface, that the tangential component of the electric field be continuous, is satisfied identically because the plasma–vacuum boundary is a flux surface.

The point $\psi = 0$ is not a true physical boundary but requires special treatment because it is a singularity in the (ψ, Θ, ϕ) coordinate system. Equations (14)–(16), (18), and (21) are in conservation form and are, therefore, easily integrated over the area inside the first flux surface to give time-advancement equations for ρ, f, g, p, and w at the center point. The velocity of the center point is purely Lagrangian and thus $u = v = 0$ there. The time-advancement equations for $x(0)$ and $y(0)$, the coordinates of the center point, are obtained by rewriting the momentum equations in conservation form and integrating these over the area inside the first flux surface. Thus,

$$[\mathscr{J}\rho_0 x_t(0)]_t = -\frac{\partial}{\partial\psi}\left\langle \mathscr{J}\rho u[(u + \Lambda)\, x_\psi + (v + \Omega)\, x_\Theta] + \frac{1}{k} P y_\Theta \right\rangle$$

and

$$[\mathscr{J}\rho_0 y_t(0)]_t = -\frac{\partial}{\partial\psi}\left\langle \mathscr{J}\rho u[(u + \Lambda)\, y_\psi + (v + \Omega)\, y_\Theta] - \frac{1}{k} P x_\Theta \right\rangle,$$

where $\langle\ \rangle$ denotes an average over a flux surface.

These equations are suitable for time integration on the fast time scale. However, to efficiently integrate over the transverse time scale we must isolate the fast wave phenomena. This is accomplished by writing an equation for the time derivative of

$$\Delta \equiv u_\psi + v_\Theta - T_t/T = \nabla \cdot \mathbf{v},$$

obtained by adding the ψ derivative of Eq. (19) to the Θ derivative of Eq. (20), and by writing an equation for the time derivative of P obtained by combining Eqs. (15), (16), (18), (3), and (4). Thus,

$$\Delta_t + \nabla \cdot (1/\rho)\, \nabla P + Q = 0, \tag{27}$$

$$P_t + (\gamma p + g^2 B_0^2)\Delta + N = 0, \tag{28}$$

where

$$Q \equiv R_\psi + S_\Theta$$

and

$$\begin{aligned} N \equiv\ & u(p + \tfrac{1}{2}g^2)_\psi + v(p + \tfrac{1}{2}g^2)_\Theta - 2\pi f g w_\Theta T^2 B_0^2 + fk^2 \mid \nabla\psi \mid^2 (fu)_\psi B_0^2 \\ & - \tfrac{1}{2} f^2 k^2 [-2\nabla\Theta \cdot \nabla\psi \Delta_\Theta + 2 \mid \nabla\psi \mid^2 \Omega_\Theta + \Delta \mid \nabla\psi \mid_\psi^2 + \Omega \mid \nabla\psi \mid_\Theta^2] B_0^2 \\ & - T_t f^2 k^2 \mid \nabla\psi \mid^2 B_0^2/T. \end{aligned} \tag{29}$$

Equations (27) and (28) contain wave motion at the fast magnetosonic wave velocity. Since the coordinate velocities have been forced to be incompressible, the fast wave compressible oscillations of the plasma will affect only the relative velocities (u, v).To lowest order in k^2 the coordinate metric has been freed from the fast wave motion.

4. Vacuum Region

To complete the boundary conditions for the plasma region equations, the magnetic pressure $P = \frac{1}{2}B^2$ must be provided on the vacuum side of the plasma–vacuum interface. This is obtained by solving an elliptic magnetostatic problem each time step in the irregularly shaped and changing vacuum region. We use a Green's function solution method [2, 10] which allows for the existence of external currents in the vacuum region.

The magnetic field in the vacuum region is represented as

$$\mathbf{B} = \frac{B_0}{2\pi} \nabla\phi \times \nabla\chi + \frac{B_0}{k} g_v \nabla\phi. \tag{30}$$

There is a singular current distribution in the vacuum region due to M external line current sources located at $\{x_m, y_m ; m = 1, M\}$,

$$\frac{1}{B_0} J = \sum_{m=1}^{M} J_m \delta(\mathbf{x} - \mathbf{x}_m). \tag{31}$$

We solve for χ using the interior Green's function

$$G(x_T, y_T \mid x_s, y_s) = \frac{1}{2k}\{\ln[(x_T - x_s)^2 + (y_T - y_s)^2] - \ln[(\epsilon x_T - x_s/\epsilon)^2 + (\epsilon y_T - y_s/\epsilon)^2]\}, \tag{32}$$

where $\epsilon \equiv (x_s^2 + y_s^2)^{1/2}/b$. Here b is the radius of a conducting wall centered about the origin.

The poloidal flux χ at a point $\mathbf{x}_T$ on the plasma–vacuum boundary is

$$\chi(\mathbf{x}_T) = \chi_w + \sum_{m=1}^{M} J_m G_{Tm} + \frac{k}{2\pi} \oint dl_s \, G_{Ts} \frac{\partial \chi}{\partial n_s}, \tag{33}$$

where the line integral is over the plasma–vacuum boundary and χ_w is the poloidal flux inside the conducting shell. We regard this as an integral equation for $\partial\chi/\partial n$ as a functional of $\chi_T = \chi(\mathbf{x}_T)$ and the shape of the interface. It is solved by approximating the line integral by many line segments Δl_s, over each of which $\partial\chi/\partial n$ is assumed constant, and thus transforming the integral Eq. (33) into a matrix equation. Thus, for $T = 1, n$,

$$\chi_T - \chi_w - \sum_{m=1}^{M} J_m G_{Tm} = \frac{k}{2\pi} \sum_{\substack{s=1,N \\ s \neq T}} \Delta l_s G_{Ts} \frac{\partial \chi}{\partial n_s} + \frac{k}{2\pi} \int_{\Delta l_T} dl_{s'} G_{Ts'} \frac{\partial \chi}{\partial n_s}.$$

Special care is necessary in the evaluation of the last "self-field" term since $| G_{Ts} | \to \infty$ as $\mathbf{x}_T \to \mathbf{x}_s$. This can be approximated by

$$\int_{\Delta l_T} dl_s G_{Ts} \frac{\partial \chi}{\partial n_s} \simeq \frac{\partial \chi}{\partial n_T} \Delta l_T \left[\left(\ln \frac{\Delta l_T}{2} - 1\right) - \ln \left| \epsilon \mathbf{x}_T - \frac{1}{\epsilon} \mathbf{x}_T \right|\right] \equiv \frac{\partial \chi}{\partial n_T} \Delta l_T \delta_T. \tag{35}$$

The integral Eq. (33) is thus reduced to the matrix equation

$$\mathbf{A} \cdot \mathbf{B} = \mathbf{C}, \tag{36}$$

where

$$C_T = \chi_T - \chi_w - \sum_{m=1}^{N} J_m G_{Tm}, \tag{37}$$

$$B_s = \frac{\partial \chi}{\partial n_s}, \tag{38}$$

$$A_{Ts} = \frac{k}{2\pi} \Delta l_s \, G_{Ts}, \qquad \text{for } T \neq s, \tag{39}$$

$$A_{TT} = \frac{k}{2\pi} \Delta l_T \, \delta_T. \tag{40}$$

Equation (36) is then solved numerically using standard $L - U$ decomposition [11].

We next consider the determination of the toroidal field constant g_v in the vacuum. This is determined by the physical requirement that the toroidal flux in the vacuum, Ψ_v, remain constant. Thus,

$$\Psi_v = \frac{1}{2\pi}\int_v d\tau \mathbf{B}\cdot\nabla\phi = \pi g_v[b^2 - T(t)^{-1}] \tag{41}$$

or

$$g_v = \frac{\Psi_v}{\pi b^2 - \pi/T(t)} \tag{42}$$

with Ψ_v a prescribed constant. On the vacuum side of the plasma boundary the total pressure

$$P = \frac{B_0^2}{2}\left[\left(\frac{k}{2\pi}\right)^2\left(\frac{\partial\chi}{\partial n}\right)^2 + g_v^2\right] \tag{43}$$

is completely determined.

The boundary conditions applicable at the plasma–vacuum interface are that the poloidal flux and total pressure are continuous;

$$[\![\chi]\!] = 0, \qquad [\![P]\!] = 0. \tag{44}$$

The second of these is needed to justify numerical differentiation of P across the plasma–vacuum interface. There is no requirement that the tangential components of the vector $\mathbf{B}$ be continuous across the plasma–vacuum interface. This reflects the fact that surface currents can arise during the course of a calculation.

The boundary condition at the outside wall, $\chi_w = \text{const}$, merely reflects the fact that poloidal flux is conserved.

5. The Finite-Difference Method

The finite-difference method has been motivated by the desire to replace the Courant stability criterion based on the fast wave velocity by one based on the transverse wave velocity. As previously discussed, there are two relevant time scales present; the ω_f^{-1} time scale of the fast compressible modes and the ω_T^{-1} time scale of the transverse modes. The motion of the grid is constrained to be incompressible and thus it occurs on the ω_T^{-1} time scale. The metric tensor and the Christoffel symbols, which are computed from the grid, also change only on the slow time scale.

The ω_f^{-1} time scale motion must be solved implicitly in order to violate the fast wave Courant stability criterion. This is easily accomplised in our formulation since the fast wave motion is contained in Eqs. (27) and (28) for Δ and P. Since the metric terms change only over the slower time scale ω_T^{-1}, they can be held constant during the implicit iteration for Δ and for P.

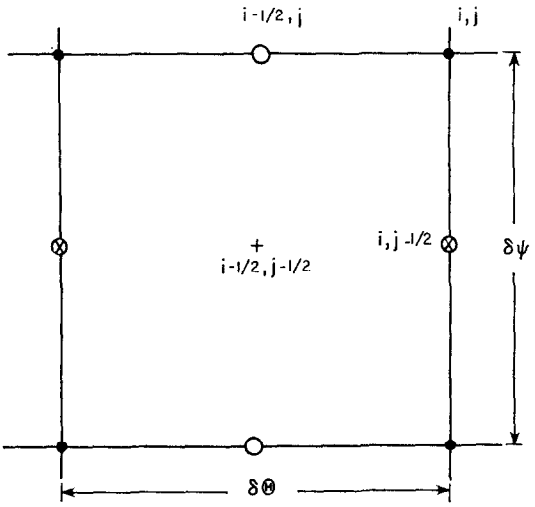

FIG. 2. Variables are defined centered at one of four grid locations: ●—x, y, $\{^{m}_{n}{}^{p}\}$; ○—u, Λ, $|\nabla\psi|^2$; ⊗—v, w, Ω, $|\nabla\Theta|^2$; +—f, ρ, g, p, P, $\nabla\Theta\cdot\nabla\psi$.

We stagger variables on the grid as shown in Fig. 2 and use a two-step partially implicit numerical method. All spatial derivatives are approximated by finite differences over a single zone spacing. Variables needed at locations other than where they are defined are obtained by averaging nearest neighbors.

The first step of our method is a fully explicit generalization of the first step of the two-step Lax–Wendroff method to a staggered grid. The time-advancement equations for all plasma variables are of the form

$$\frac{\partial A}{\partial t} + B = 0, \tag{45}$$

where B contains all the spatial derivatives. Denoting $A(j\delta\psi, i\delta\Theta, n\delta t)$ by $A^n_{i,j}$, we use the prescription

$$A^{n+1/2}_{i,j} = (1-\sigma)\,A^n_{i,j} + \tfrac{1}{4}\sigma(A^n_{i+1,j} + A^n_{i-1,j} + A^n_{i,j-1} + A^n_{i,j+1}) - \tfrac{1}{2}\delta t\,B^n_{i,j}\,. \tag{46}$$

Here σ is an averaging parameter which influences the accuracy and the stability of the overall method. Typically, a value of σ equal to 0.25 is used.

In step 2 we first solve implicitly for the rapidly varying quantities P and Δ and then use these to advance the other variables. The finite-difference forms of Eqs. (27) and (28) are

$$\begin{aligned}\frac{\Delta^{n+1}-\Delta^n}{\delta t} &+ \left(\frac{|\nabla\psi|^2}{\rho}\right)^{n+1/2}\hat{P}_{\psi\psi} + 2\left(\frac{\nabla\Theta\cdot\nabla\psi}{\rho}\right)^{n+1/2}\hat{P}_{\psi\Theta} \\ &+ \left(\frac{|\nabla\Theta|^2}{\rho}\right)^{n+1/2}\hat{P}_{\Theta\Theta} + \left[\left(\frac{|\nabla\psi|^2}{\rho}\right)^{n+1/2}_{\psi} + \left(\frac{\nabla\Theta\cdot\nabla\psi}{\rho}\right)^{n+1/2}_{\Theta}\right]\hat{P}_{\psi} \\ &+ \left[\left(\frac{\nabla\Theta\cdot\nabla\psi}{\rho}\right)^{n+1/2}_{\psi} + \left(\frac{|\nabla\Theta|^2}{\rho}\right)^{n+1/2}_{\Theta}\right]\hat{P}_{\Theta} + Q^{n+1/2} = 0\end{aligned} \tag{47}$$

and

$$\frac{P^{n+1} - P^n}{\delta t} + (\gamma p + B_0{}^2 g^2)^{n+1/2} \hat{\Delta} + N^{n+1/2} = 0, \tag{48}$$

where $\hat{F} \equiv [\Phi F^{n+1} + (1 - \Phi) F^n]$. Here Φ is a parameter measuring the implicitness of the scheme. A value of $\Phi = 0$ corresponds to being fully explicit, while $\Phi = 1$ solves these two equations fully implicitly. A linear analysis shows that unconditional numerical stability for this part of the calculation should result for values of $\Phi \geqslant 0.5$. A value of $\Phi = 0.5$ gives complete time centering and hence the smallest numerical truncation error, but is only neutrally stable. In practice, we typically use $\Phi = 0.6$. After spatial differencing and eliminating Δ^{n+1} from Eqs. (47) and (48), we obtain

$$\begin{aligned} P_{i,j}^{n+1} - a_{i,j}\Phi^2 \Big[& \frac{c_{i,j}}{\delta\psi^2} (P_{i,j+1}^{n+1} - 2P_{i,j}^{n+1} + P_{i,j-1}^{n+1}) \\ & + \frac{d_{i,j}}{4\delta\psi\delta\Theta} (P_{i+1,j+1}^{n+} - P_{i+1,j-1}^{n+1} - P_{i-1,j+1}^{n+} + P_{i-1,j-1}^{n+1}) \\ & + \frac{e_{i,j}}{(\delta\Theta)^2} (P_{i+1,j}^{n+1} - 2P_{i,j}^{n+1} + P_{i-1,j}^{n+1}) + \frac{h_{i,j}}{2\delta\psi} (P_{i,j+1}^{n+1} - P_{i,j-1}^{n+1}) \\ & + \frac{l_{i,j}}{2\delta\Theta} (P_{i+1,j}^{n+1} - P_{i-1,j}^{n+1}) \Big] + K_{i,j} = 0, \end{aligned} \tag{49}$$

where

$$a_{i,j} \equiv \delta t(\gamma p + g^2 B_0{}^2)_{i,j}^{n+1/2}, \qquad c_{i,j} \equiv \delta t \left(\frac{|\nabla\psi|^2}{\rho}\right)_{i,j}^{n+1/2},$$

$$d_{i,j} \equiv 2\delta t \left(\frac{\nabla\Theta \cdot \nabla\psi}{\rho}\right)_{i,j}^{n+1/2}, \qquad e_{i,j} \equiv \delta t \left(\frac{|\nabla\Theta|^2}{\rho}\right)_{i,j}^{n+1/2},$$

$$h_{i,j} \equiv \delta t \left[\left(\frac{|\nabla\psi|^2}{\rho}\right)_{\psi} + \left(\frac{\nabla\Theta \cdot \nabla\psi}{\rho}\right)_{\Theta}\right]_{i,j}^{n+1/2},$$

$$l_{i,j} \equiv \delta t \left[\left(\frac{\nabla\Theta \cdot \nabla\psi}{\rho}\right)_{\psi} + \left(\frac{|\nabla\Theta|^2}{\rho}\right)_{\Theta}\right]_{i,j}^{n+1/2},$$

$$\begin{aligned} K_{i,j} \equiv & -P_{i,j}^n - \Phi(1 - \Phi)\, a_{i,j}(c_{i,j}P_{\psi\psi}^n + d_{i,j}P_{\Theta\psi}^n + e_{i,j}P_{\Theta\Theta}^n + h_{i,j}P_{\psi}{}^n + l_{i,j}P_{\Theta}{}^n) \\ & - \Phi a_{i,j}\delta t Q_{i,j}^{n+1/2} + a_{i,j}\Delta^n + \delta t N_{i,j}^{n+1/2}. \end{aligned} \tag{50}$$

Equation (49) is solved each time step according to the successive over relaxation iteration scheme [12–15]

$$\begin{aligned} \tilde{P}_{i,j}^{n+1} = (1 - \omega)\, P_{i,j}^{n+1} + \frac{\omega}{[1 + 2a\Phi^2(c/\delta\psi^2 + e/\delta\Theta^2)]} \Big[& \frac{ac\Phi^2}{\delta\psi^2} (P_{i,j+1}^{n+1} + \tilde{P}_{i,j-1}^{n+1}) \\ & + \frac{ae\Phi^2}{\delta\Theta^2} (P_{i+1,j}^{n+} + \tilde{P}_{i-1,j}^{n+1}) \\ & + \frac{ad\Phi^2}{4\delta\psi\delta\Theta} (P_{i+1\,j+1}^{n+1} - \tilde{P}_{i+1\,j-1}^{n+1} - P_{i-1,j+1}^{n+1} + \tilde{P}_{i-1,j-1}^{n+1}) \\ & + \frac{ah\Phi^2}{2\delta\psi} (P_{i,j+1}^{n+1} - \tilde{P}_{i,j-1}^{n+1}) + \frac{al\Phi^2}{2\delta\Theta} (P_{i+1,j}^{n+1} - \tilde{P}_{i-1,j}^{n+1}) - K_{i\,j} \Big]. \end{aligned} \tag{51}$$

Here $\tilde{P}^{n+1}$ denotes the new value for the particular iteration, and cycling is implied in the directions of increasing i and j. Precise statements regarding the rate of convergence of this method are impossible to make since this requires knowledge of the spectral radius of the coefficient matrix, the elements of which are functions of time and space. However, analogy with Laplace's equation on a rectangular mesh suggests convergence for the successive overrelaxation parameter $0 < \omega < 2$ with the optimal ω value somewhat exceeding unity. In practice, the optimal ω is chosen by experimentation, and convergence with $\omega = 1.7$ is found to be quite rapid (10–20 iterations). The iteration is repeated until some criterion of convergence is satisfied. We typically require that

$$\max_{\substack{i\in(1,I)\\ j\in(1,J)}} | \tilde{P}_{i,j}^{n+1} - P_{i,j}^{n+1} | \leqslant 10^{-5} \frac{1}{IJ} \sum_{\substack{i\in(1,I)\\ j\in(1,J)}} | \tilde{P}_{i,j} |^{n+1}. \tag{52}$$

Before beginning this iteration, we compute x^{n+1} and y^{n+1} at the boundary and throughout the plasma using the explicit finite-difference form of Eqs. (2) and (3),

$$\frac{(x^{n+1} - x^n)}{\delta t} = (x_\psi \Lambda + x_\Theta \Omega)^{n+1/2},$$
$$\frac{(y^{n+1} - y^n)}{\delta t} = (y_\psi \Lambda + y_\Theta \Omega)^{n+1/2}. \tag{53}$$

With x^{n+1} and y^{n+1} known on the boundary, the previously described vacuum calculation gives $P_{i,j}^{n+1}$ on the vacuum side of the plasma–vacuum interface. These vacuum values of $P_{i,j}^{n+1}$ serve as the outer boundary values for the iteration, Eq. (51).

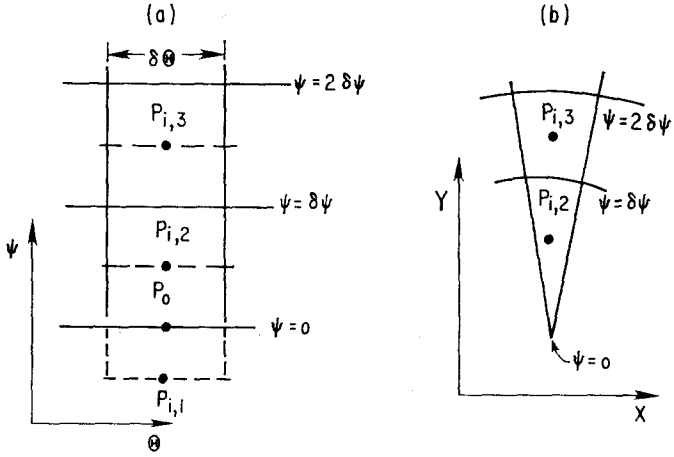

FIG. 3. Origin of coordinate system in (a) $\psi - \Theta$ space and (b) $x - y$ space. A fictitious row of variables $P_{i,-1}$ is defined so that proper values of $P_{i,1}$, $P_{i,0}$, and $P_{i,-1}$ will result when the interior

Boundary values for $P_{i,j}^{n+1}$ must also be supplied at the inner boundary $j = 1$ (see Fig. 3). We first define P_0^{n+1} at the center point from $P_0^{n+1} = p_0^{n+1} + \frac{1}{2}B_0^2 g_0^2$ (since $| \nabla\psi |^2 = 0$ at $\psi = 0$). What the iteration formulas require, though, is $P_{i,1}^{n+1}$ and not P_0^{n+1}. We, therefore, define "fictitious" values by

$$P_{i,1}^{n+1} = (8/3)\, P_0^{n+1} + (1/3)\, P_{i,3}^{n+1} - 2P_{i,2}^{n+1}.$$

These yield the correct values of $P_{\psi\psi}$, $P_{\Theta\psi}$, and P_ψ for points on surface $j = 2$ when the regular interior centered difference formulas are used.

When advanced values of $P_{i,j}^{n+1}$ are obtained by iterating Eq. (51), the $\Delta_{i,j}^{n+1}$ are obtained from Eq. (47). The momentum Eqs. (19) and (20) are then advanced using

$$\frac{(u + \Lambda)^{n+1} - (u + \Lambda)^n}{\delta t} + \left(\frac{| \nabla\psi |^2}{\rho}\right)^{n+1/2} \hat{P}_\psi + \left(\frac{\nabla\Theta \cdot \nabla\psi}{\rho}\right)^{n+1/2} \hat{P}_\Theta + R^{n+1/2} = 0, \tag{55}$$

$$\frac{(v + \Omega)^{n+1} - (v + \Omega)^n}{\delta t} + \left(\frac{\nabla\Theta \cdot \nabla\psi}{\rho}\right)^{n+1/2} \hat{P}_\psi + \left(\frac{| \nabla\Theta |^2}{\rho}\right)^{n+1/2} \hat{P}_\Theta + S^{n+1/2} = 0. \tag{56}$$

The remaining equations for $\tilde{\rho}$, f, $\tilde{g}$, $\tilde{p}$, and $\tilde{\rho}w$ are of the form

$$a_t + (au)_\psi + (av)_\Theta = 0 \tag{57}$$

and are evaluated as

$$\frac{a^{n+1} - a^n}{\delta t} + (au)_\psi^{n+1/2} + (av)_\Theta^{n+1/2} = 0, \tag{58}$$

where centered conservation differencing is used and

$$\begin{aligned} u^{n+1/2} &\equiv (u^{n+1} + u^n)/2, \\ v^{n+1/2} &\equiv (v^{n+1} + v^n)/2. \end{aligned} \tag{59}$$

These new, implicitly determined values for the velocity are used in Eq. (58) along with the explicitly predicted values of the densities obtained from Eq. (46). Physically, the compressible wave motion is being treated implicitly but the incompressible motion and the material convection are being treated explicitly. Since the incompressible motion is still treated by explicit differencing, the Courant stability criteria for the incompressible (transverse) waves,

$$\delta t \leqslant (\delta x/2^{1/2} c_T)[\sigma(1 - \sigma)]^{1/2}, \tag{60}$$

must be obeyed. Since $c_T \sim c_f(Rq/a)^{-1}$, the maximum allowable time step is greatly increased over that for a fully explicit method.

6. Applications

A. *Linear Eigenmodes of Circular Cross-Section Tokamaks*

The complete spectrum of linear axisymmetric ideal MHD eigenmodes of a circular cross-section cylindrical tokamak of radius a inside a circular perfectly conducting shell of radius b can be computed accurately by using an established numerical procedure such as that described in [1].

We show in Fig. 4 some of the eigenvalues $\Omega = \omega a(\rho_0)^{1/2}/B_0$ with poloidal periodicity $m = 4$ for an equilibrium with $a = 1$, $b = 1.1055$, toroidal periodicity length $L = 2\pi$, $\rho_0 = 1$, $B_\theta/B_0 = r/Lq$, $q = 2.5$, and $P_0 = 0.01[1 - (r/a)^2]B_0^2$. The modes Ω

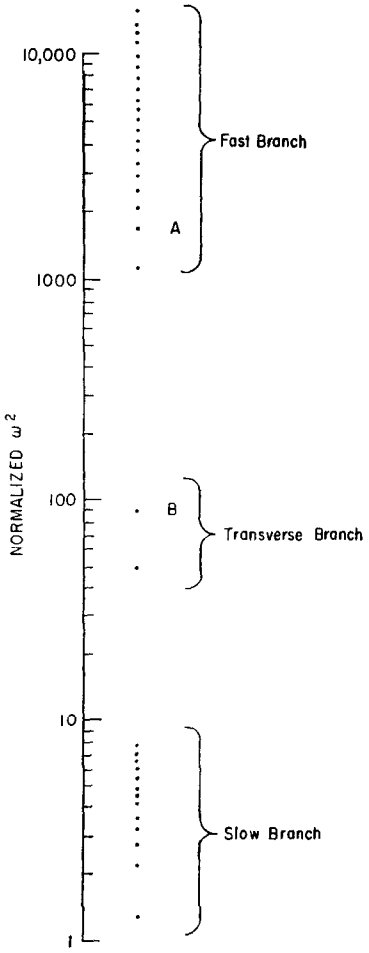

FIG. 4. Spectrum of axisymmetric eigenmodes with azimuthal wave number 4, Modes denoted by A and B will be examined closer.

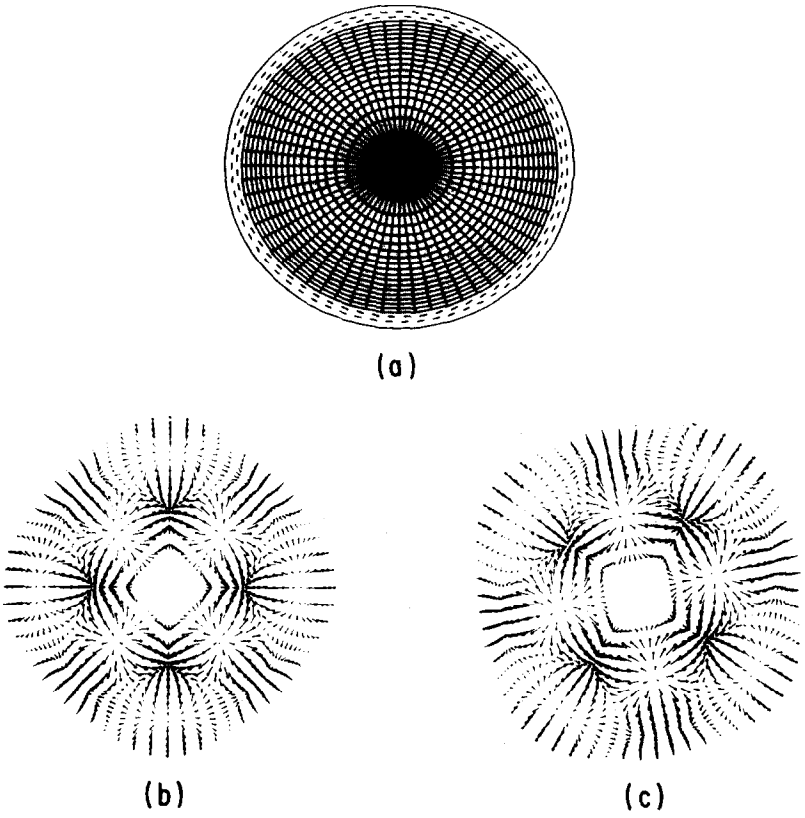

FIG. 5. Fast eigenmodes simulation. (a) Finite difference grid, (b) velocity vectors at time $t = 0$, (c) $t = 4.82$. (d) perturbed density versus time at $I = 5$, $J = 14$, (e) perturbed toroidal flux density versus time at $I = 5$, $J = 14$.

divide into three groupings which we denote as the slow branch, the transverse branch, and the fast branch.

In order to provide a check on the accuracy of our numerical solution procedure, we set up a numerical experiment in which we follow the temporal development of a system which has been initially prepared in an exact linear eigenmode. As long as $B_1 \ll B_0$, $p_1 \ll p_0$, etc., the nonlinear terms in the equations are unimportant and the computed solutions should exhibit sinusoidal time dependence with frequency Ω.

Figure 5a shows the equal-area finite-difference mesh which is used in the calculation. It is initially prepared in the eigenmode labeled A in Fig. 4. There are 18 zones in the radial direction and 60 in the Θ direction. The dotted lines are two flux surfaces in the vacuum region, and the outer circle represents a perfectly conducting vacuum wall. Figure 5b shows the velocity vectors at the initial time $t = 0$. We use a δt of 0.008, the largest allowed by the Courant stability criteria based on the fast waves for

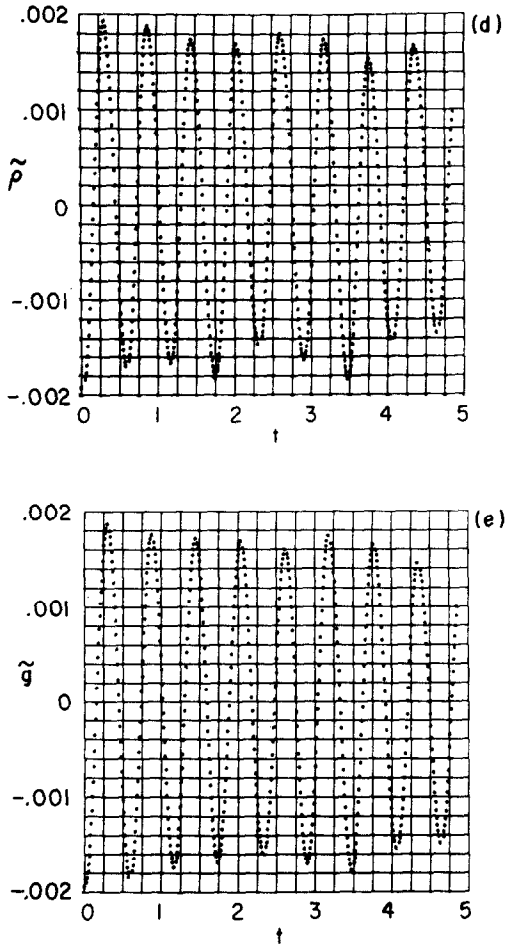

FIG. 5—*Continued*

this finite-difference mesh. The theoretical period of the oscillation is $\tau = 0.56$. Figure 5c shows the velocity vectors at the end of the calculation, $t = 4.82$, after almost 8 oscillation periods. The similarity between Figs. 5b and c is remarkable, the primary difference being a rotation due to the fact that we have not computed for an integral number of oscillation periods. This alone is a qualitative verification of the accuracy of the numerical methods.

Figures 5d and e show the time histories of the density and the toroidal field at a given location (the fourteenth flux surface from the center and the fifth theta surface from the horizontal). There is some minor attenuation and irregularity due to the finite-difference mesh but the overall resemblance of these waveforms to perfect sinusoids of period $\tau = 0.56$ is quite good.

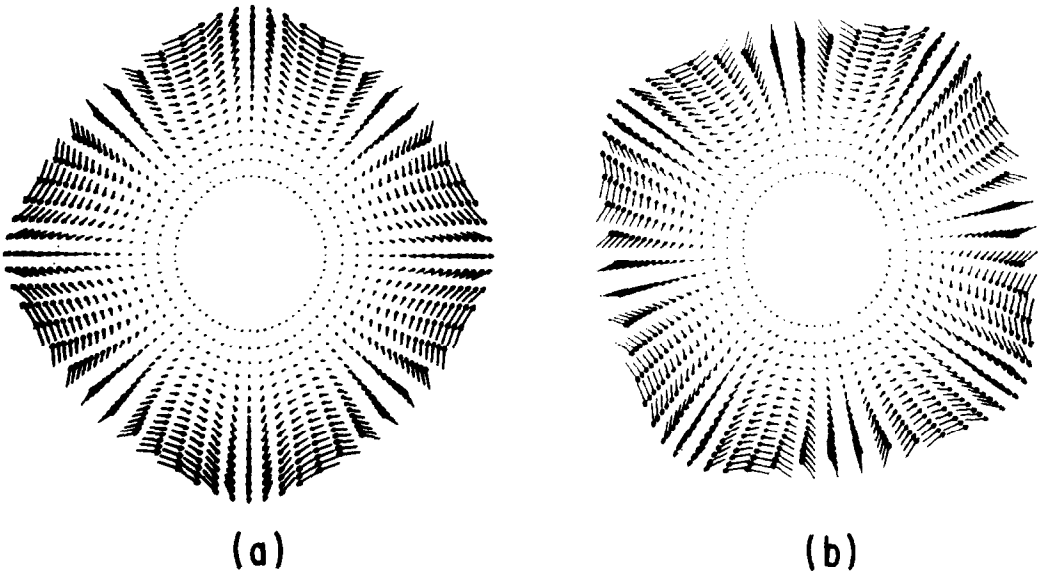

FIG. 6. Transverse eigenmode simulation. (a) Velocity vectors at time $t = 0$ and (b) $t = 47.9$, (c) $\nabla\psi$ component of velocity versus time at $I = 5$, $J = 8$, (d) perturbed $| \nabla\psi |^2$ versus time at $I = 5$, $J = 8$, (e) perturbed density versus time at $I = 5$, $J = 8$.

Figure 6 shows the results of a similar calculation initially prepared in the eigenmode labeled B in Fig. 4. This calculation is again run for 600 cycles, but the average time step used is approximately 10 times larger than that used in the calculation of Fig. 5. The theoretical period of this oscillation is $\tau = 13.8$. Figure 6a shows the initial velocity vectors for this calculation and Fig. 6b shows the velocity vectors at time 48.0, after 600 cycles or almost four oscillation periods. The resemblance between these two figures is again extraordinary. Figures 6c–e present an interesting comparison. They represent the time histories of the $\nabla\psi$ component of the velocity, the metric tensor component $| \nabla\psi |^2$, and the plasma density at a given location, this time the eighth flux surface from the center and the fifth theta surface from the horizontal. From Fig. 6c we see that the velocity consists of two components, one rapidly varying and the other slowly varying. The slowly varying component is largest in amplitude and corresponds to the slow nearly incompressible eigenmode we are trying to compute. The smaller amplitude high-frequency component arises primarily from the inexactness of the finite-difference initial conditions.

Examination of Fig. 6d shows that there is no high-frequency component in the metric tensor component $| \nabla\psi |^2$. Figure 6e similarly shows that there is little or no low-frequency component in the time variation of the density. Thus, the separation of the velocity into a slowly varying incompressible part and a rapidly varying compressible part has been successful.

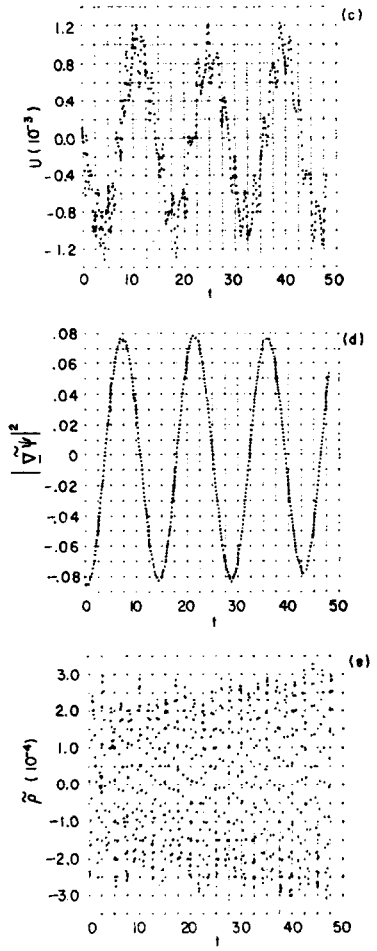

FIG. 6—*Continued*

B. *Motion of a Rectangular Cross-Section Cylindrical Tokamak*

It has been shown analytically by Rosen [16] that a free-boundary straight plasma column with a rectangular cross section, carrying a uniform axial current, is unstable to an axisymmetric ($n = 0$) mode which is primarily a rigid translation ($m = 1$) but with a small additional $m = 3$ perturbation superimposed. This calculation is extended in [9] to give all the normal modes in a rectangular cross-section plasma. The simulation of this instability is illustrated in Figs. 7 and 8. Figure 7a shows the geometry at the start of this calculation. The 8 external currents shown in the vacuum region maintain the rectangular shape of the equilibrium cross section.

The equilibrium is perturbed with an $m = 1$ and an $m = 3$ component and the subsequent motion is computed. Figures 7b–g illustrate the plasma configuration and the velocity vectors after computing for 800 cycles, 1600 cycles, and 2400 cycles.

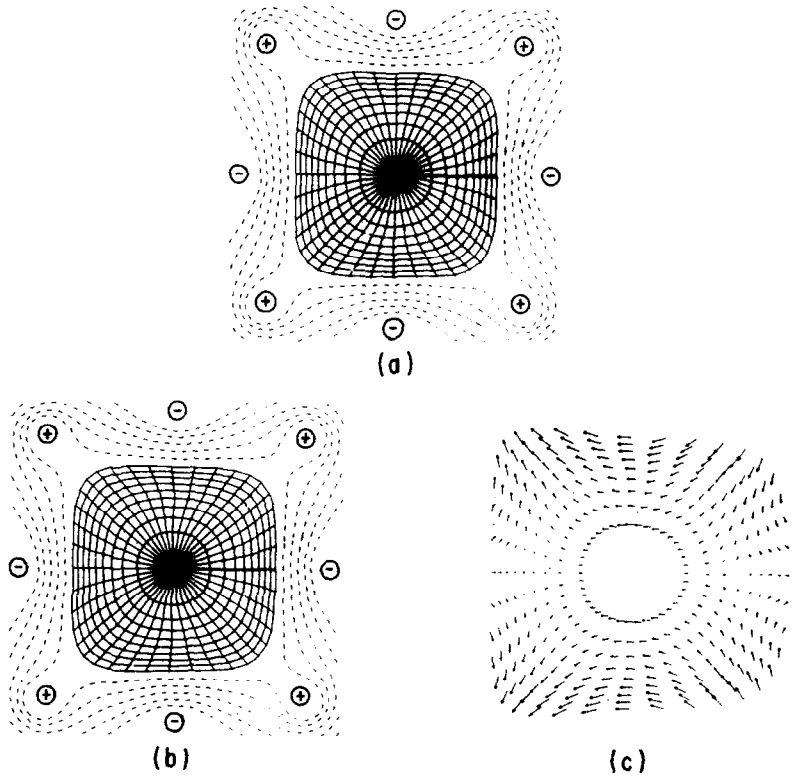

FIG. 7. Rectangular instability simulation. (a) Initial finite difference grid. Dotted lines are vacuum flux surfaces. (b) Grid at $t = 112$; (c) velocity vectors at $t = 112$. (d) and (e) $t = 213$; (f) and (g) $t = 282$.

The time step used was $\delta t = 0.1$, 12 times larger than that allowed by the fast wave Courant condition.

All of the essential features of this calculation can be interpreted using Fig. 8 which is a graph of the x-coordinate of the magnetic axis versus time. The initial perturbation of the equilibrium was mostly a linear superposition of two modes, one stable $m = 3$ mode with period $\tau = 25$ and the other an unstable $m = 1$ mode. As time progresses, the amplitude of the stable mode remains about the same (this is not obvious on a semilog plot) but the amplitude of the unstable mode grows exponentially. The unstable mode soon dominates the calculation. After about 1400 cycles the exponential growth begins to saturate. The velocity of the center point decreases and eventually reverses direction. This calculation was stopped at this point. Had we continued we would have found that the center point would continue to oscillate about some position intermediate between its starting location and the turning point shown. The exponential growth rate predicted by the linear theory is also plotted in Fig. 8. The agreement with the computed result is remarkable.

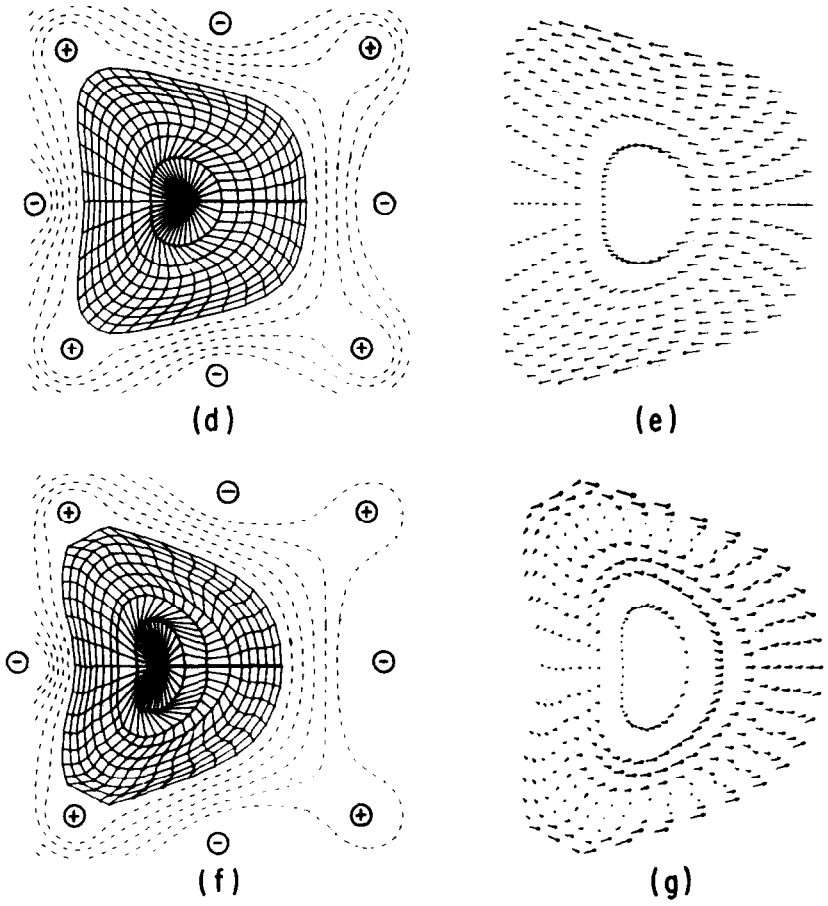

FIG. 7—*Continued*

7. CONCLUSIONS

A new method has been presented for calculating the linear and the nonlinear axisymmetric transient dynamics of tokamak systems with realistic parameters and arbitrary shape. We list here its most significant features.

1. A nonorthogonal coordinate system with a time varying metric is utilized. This allows phenomena occurring on the fast and transverse time scales to be approximately isolated and enables the characteristics of the MHD equations to be well represented.

2. Grid points move in such a way that magnetic surfaces remain grid lines and the area of each computational zone remains constant. This is accomplished without resorting to a separate computational rezone step. This has the effect of

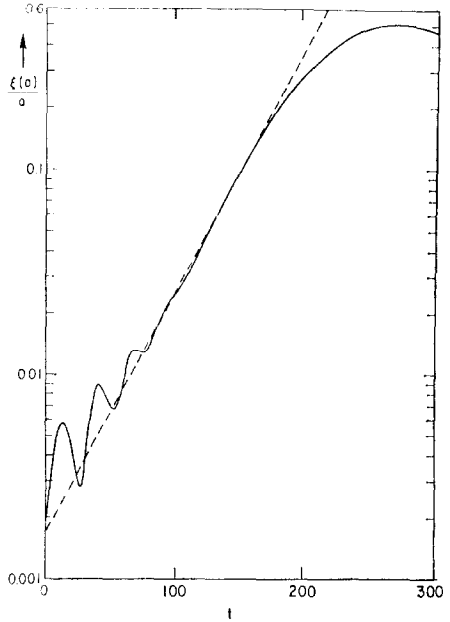

FIG. 8. Normalized vertical displacement of magnetic axis versus time for rectangular instability. Initially both stable and unstable modes are present. The unstable mode soon dominates. The mode saturates and direction reversal occurs. The dashed curve is the prediction of linear theory.

minimizing convection across grid lines while maintaining a grid configuration free from rotation and extreme distortion.

(3) All equations are time centered, and the (ψ, Θ) grid on which derivatives are taken remains equally spaced and undistorted. This allows use of a difference scheme which remains second-order accurate in δt, $\delta\psi$, and $\delta\Theta$.

4. Realistic two-dimensional geometries can be considered where the effects of both external currents and conducting walls are included in the determination of the behavior of the plasma.

5. Our method includes the effects of plasma compressibility but does not have the stringent time step restriction associated with the Courant–Friedrichs–Lewy condition based on the fast compressible wave velocity. This is accomplished by treating the compressible motion implicitly.

6. Verification of the accuracy of the method in the linear regime is demonstrated by computing both stable and unstable motions of the plasma and comparing our results with those of an established spectrum code and with analytic results.

Application of the dynamical grid method to study the use of passive feedback to control axisymmetric instabilities in actual tokamak experiments will soon appear [17]. This general method of using a time-dependent coordinate transformation to accurately represent and to separate dynamic phenomena in tokamaks is presently being

extended to a fully three-dimensional nonlinear ideal MHD model applicable for phenomena on the poloidal Alfvén time scale and to a two-dimensional tokamak transport model which should be used on a resistive time scale.

APPENDIX: TOROIDAL GEOMETRY

We use coordinates similar to those described in Sec. 2 with the primary difference being that now

$$| \nabla\phi |^2 = \frac{1}{x^2}, \qquad \mathscr{J} \equiv (\nabla\psi \times \nabla\Theta \cdot \nabla\phi)^{-1} = \frac{x}{2\pi T(t)}. \tag{A-1}$$

Here x is the distance from the major axis and $T(t)$ is again a spatial constant determined by the requirement that $u = 0$ at the plasma–vacuum interface. This system still has the property that each area $\delta\psi\delta\Theta$ is the same. All of the relations between basis vectors given in the text hold when the substitution $k \to 1/x$ is made. There are now six new nonzero Christoffel symbols. These are given by

$$\begin{Bmatrix} 3 \\ 1\ 3 \end{Bmatrix} = \begin{Bmatrix} 3 \\ 3\ 1 \end{Bmatrix} = \frac{x_\psi}{x},$$

$$\begin{Bmatrix} 3 \\ 2\ 3 \end{Bmatrix} = \begin{Bmatrix} 3 \\ 3\ 2 \end{Bmatrix} = \frac{x_\Theta}{x},$$

$$\begin{Bmatrix} 1 \\ 3\ 3 \end{Bmatrix} = \frac{-1}{2}[| \nabla\psi |^2 (x^2)_\psi + \nabla\Theta \cdot \nabla\psi (x^2)_\Theta],$$

$$\begin{Bmatrix} 2 \\ 3\ 3 \end{Bmatrix} = \frac{-1}{2}[\nabla\Theta \cdot \nabla\psi (x^2)_\psi + | \nabla\Theta |^2 (x^2)_\Theta]. \tag{A-2}$$

The magnetic field is now given by

$$\begin{aligned} \mathbf{B} &= B_0[f(\psi, t)\, \nabla\phi \times \nabla\psi + Rg(\psi, \Theta, t)\, \nabla\phi], \\ x^2 B^2 &= B_0^2[f^2 | \nabla\psi |^2 + R^2 g^2]. \end{aligned} \tag{A-3}$$

Here R is a normalization constant such that RB_0/x is the externally imposed toroidal field. By redefining certain variables, we obtain an almost identical set of equations as those solved in the text.

In the plasma region

$$\bar{\rho}_t + (\bar{\rho}u)_\psi + (\bar{\rho}v)_\Theta = 0, \tag{A-4}$$

$$f_t + (fu)_\psi = 0, \tag{A-5}$$

$$\bar{g}_t + (\bar{g}u)_\psi + (\bar{g}v - 2\pi f w)_\Theta = 0, \tag{A-6}$$

$$\bar{p}_t + (\bar{p}u)_\psi + (\bar{p}v)_\Theta = 0, \tag{A-7}$$

$$(u + \Lambda)_t + \frac{1}{\rho} \mid \nabla\psi \mid^2 \bar{P}_\psi + \frac{1}{\rho} \nabla\Theta \cdot \nabla\psi \, \bar{P}_\Theta + R = 0, \tag{A-8}$$

$$(v + \Omega)_t + \frac{1}{\rho} \nabla\Theta \cdot \nabla\psi \, \bar{P}_\psi + \frac{1}{\rho} \mid \nabla\Theta \mid^2 \bar{P}_\Theta + S = 0, \tag{A-9}$$

$$W_t + (Wu)_\psi + (Wv)_\Theta - B_0{}^2 \frac{2\pi f T}{Rx} \bar{g}_\Theta + 2W(u + \Lambda) \begin{Bmatrix} 3 \\ 1 \; 3 \end{Bmatrix} + \left(2W(v + \Omega) - B_0{}^2 \frac{2\pi f T}{Rx} \bar{g}\right) \begin{Bmatrix} 3 \\ 2 \; 3 \end{Bmatrix} = 0, \tag{A-10}$$

$$x_t = x_\psi \Lambda + x_\Theta \Omega, \tag{A-11}$$

$$y_t = y_\psi \Lambda + y_\Theta \Omega, \tag{A-12}$$

where

$$\begin{aligned} &\bar{\rho} \equiv \frac{\rho}{T} \frac{x}{R}, \qquad \bar{p} \equiv \frac{x}{RT} p^{1/\gamma}, \qquad \bar{g} \equiv \frac{R}{x} \frac{g}{T}, \qquad W \equiv \bar{\rho}\omega, \\ &P \equiv \frac{B_0{}^2}{2} \left(\frac{f^2}{x^2} \mid \nabla\psi \mid^2 + T^2 \bar{g}^2\right) + p, \qquad \bar{P} \equiv P - \frac{B_0{}^2}{2} \frac{R^2}{x^2} g_0{}^2, \end{aligned} \tag{A-13}$$

$$\begin{aligned} \Lambda &\equiv T\xi_\Theta - \pi T_t\{[x - x(0)]\, y_\Theta - [y - y(0)]\, x_\Theta\}, \\ \Omega &\equiv -T\xi_\psi + \pi T_t\{[x - x(0)]\, y_\psi - [y - y(0)]\, x_\psi\}, \end{aligned}$$

$$\begin{aligned} R \equiv\; & v(u + \Lambda)_\Theta + u(u + \Lambda)_\psi + (u + \Lambda)\Lambda_\psi + (v + \Omega)\Lambda_\Theta \\ & + (u + \Lambda)^2 \begin{Bmatrix} 1 \\ 1 \; 1 \end{Bmatrix} + (v + \Omega)^2 \begin{Bmatrix} 1 \\ 2 \; 2 \end{Bmatrix} + 2(u + \Lambda)(v + \Omega) \begin{Bmatrix} 1 \\ 2 \; 1 \end{Bmatrix} \\ & - \frac{1}{\rho} \left(\frac{2\pi B_0 f T}{x}\right)^2 \begin{Bmatrix} 1 \\ 2 \; 2 \end{Bmatrix} + \left[w^2 - \left(\bar{g}^2 - g_0{}^2 \frac{R^2}{x^2 T^2}\right) \frac{B_0{}^2 T^2}{\rho x^2}\right] \begin{Bmatrix} 1 \\ 3 \; 3 \end{Bmatrix}, \end{aligned} \tag{A-14}$$

$$\begin{aligned} S \equiv\; & v(v + \Omega)_\Theta + u(v + \Omega)_\psi + (u + \Lambda)\Omega_\psi + (v + \Omega)\Omega_\Theta \\ & + (u + \Lambda)^2 \begin{Bmatrix} 2 \\ 1 \; 1 \end{Bmatrix} + (v + \Omega)^2 \begin{Bmatrix} 2 \\ 2 \; 2 \end{Bmatrix} + 2(u + \Lambda)(v + \Omega) \begin{Bmatrix} 2 \\ 1 \; 2 \end{Bmatrix} \\ & - \frac{1}{\rho} \left(\frac{2\pi B_0 f T}{x}\right)^2 \begin{Bmatrix} 2 \\ 2 \; 2 \end{Bmatrix} + \left[w^2 - \left(\bar{g}^2 - g_0{}^2 \frac{R^2}{x^2 T^2}\right) \frac{B_0{}^2 T^2}{\rho x^2}\right] \begin{Bmatrix} 2 \\ 3 \; 3 \end{Bmatrix} \\ & + \frac{B_0{}^2}{2\rho} \left(\frac{f^2}{\mathscr{J}^2}\right)_\Theta. \end{aligned} \tag{A-15}$$

Straightforward manipulation gives

$$\bar{P}_t + (B_0{}^2 T^2 \bar{g}^2 + \gamma p)\Delta + N = 0. \tag{A-16}$$

As before, we take the derivative of Eq. (A-8) with respect to ψ and of (A-9) with respect to Θ and add. Then

$$\Delta_t + \nabla \cdot \frac{1}{\rho} \nabla\bar{P} + Q = 0. \tag{A-17}$$

Here

$$\Delta \equiv u_\psi + v_\Theta - \frac{T_t}{T} = \nabla \cdot \mathbf{v} - \frac{x_\psi}{x}(u + \Lambda) - \frac{x_\Theta}{x}(v + \Omega) \tag{A-18}$$

is the part of the divergence of the velocity not associated with expansion or compression in major radius,

$$Q = R_\psi + S_\Theta ,$$

$$\begin{aligned} N = {} & u(p + \tfrac{1}{2}T^2\bar{g}^2B_0^2)_\psi + v(p + \tfrac{1}{2}T^2\bar{g}^2B_0^2)_\Theta - 2\pi f\bar{g}w_\Theta B_0^2T^2 \\ & + f\frac{B_0^2}{x^2}\,|\,\nabla\psi\,|^2\,(fu)_\psi - \frac{B_0^2}{2}\frac{f^2}{R^2}\left[-\frac{2R^2}{x^2}\,\nabla\Theta\cdot\nabla\psi\,\Lambda_\Theta + \frac{2R^2}{x^2}\,|\,\nabla\psi\,|^2\,\Omega_\Theta\right. \\ & \left. + \Lambda\left(\frac{R^2}{x^2}\,|\,\nabla\psi\,|^2\right)_\psi + \Omega\left(\frac{R^2}{x^2}\,|\,\nabla\psi\,|^2\right)_\Theta\right] - \frac{T_t}{T}\frac{B_0^2f^2}{x^2}\,|\,\nabla\psi\,|^2 \\ & + \gamma p\left(\begin{Bmatrix}3\\1\;3\end{Bmatrix}(u + \Lambda) + \begin{Bmatrix}3\\2\;3\end{Bmatrix}(v + \Omega)\right) - \frac{B_0^2R^2g_0^2}{x^2}\left(\frac{x_\psi}{x}\Lambda + \frac{x_\Theta}{x}\Omega\right). \end{aligned} \tag{A-19}$$

In the vacuum region the poloidal flux is obtained with the infinite medium toroidal Green's function

$$G_{Ts} = \frac{-2x_Tx_s}{[(x_T + x_s)^2 + (y_T - y_s)^2]^{1/2}}\left(\frac{(2 - k^2)\,K(k^2) - 2E(k^2)}{k^2}\right), \tag{A-20}$$

where

$$k^2 \equiv \frac{4x_Tx_s}{[(x_T + x_s)^2 + (y_T - y_s)^2]}$$

and K and E are elliptic integrals of the first and second kind. The poloidal flux in the vacuum is given by

$$\chi(\mathbf{x}_T) = \chi_w + \sum_{m=1}^{M} J_mG_{Tm} + \frac{1}{2\pi}\oint\frac{dl_s}{x_s}\,G_{Ts}\frac{\partial\chi}{\partial n_s}, \tag{A-21}$$

where the line integrals are now evaluated over the plasma–vacuum interface and the wall. As before, we approximate these integrals by sums, taking special care in evaluating the "self-field" term [see Eq. (40)]

$$A_{TT} = \frac{\Delta l_T}{2\pi}\left[\ln\left(\frac{\Delta l_T}{16x_T}\right) + 1\right].$$

The toroidal equivalent to Eq. (42) is

$$g_v = \frac{\Psi_v}{R\int dl\cdot\hat{y}\ln x}.$$

REFERENCES

1. M. S. CHANCE, J. M. GREENE, R. C. GRIMM, AND J. L. JOHNSON, *Nuclear Fusion* **17** (1977), 65.
2. R. WHITE, D. MONTICELLO, M. N. ROSENBLUTH, H. R. STRAUSS, AND B. B. KADOMTSEV, "Plasma Physics and Controlled Nuclear Fusion Research, 1974," Vol. I, p. 495. IAEA, Vienna, 1975.
3. H. R. STRAUSS, *Phys. Fluids* **19** (1976), 134.
4. D. POTTER, "Methods in Computational Physics," Vol. 16, p. 43, Academic Press, New York, 1976.
5. J. A. WESSON AND A. SYKES, "Plasma Physics and Controlled Nuclear Fusion Research, 1974," Vol. I, p. 449, IAEA, Vienna, 1975.
6. W. SCHNEIDER AND G. BATEMAN, "Plasma Physics and Controlled Nuclear Fusion Research, 1974," Vol. I, p. 429, IAEA, Vienna, 1975.
7. G. BATEMAN, W. SCHNEIDER, AND W. GROSSMANN, *Nuclear Fusion* **14** (1974), 669.
8. J. BRACKBILL, "Methods in Computational Physics," Vol. 16, p. 1, Academic Press, New York, 1976.
9. S. C. JARDIN, "Time Integration of the Ideal MHD Equations in 2D Tokamak Geometry," Ph.D. Thesis, Princeton University, 1976.
10. B. M. MARDER, *Phys. Fluids* **17** (1974), 634.
11. G. DALQUIST, "Numerical Methods," Prentice-Hall, Englewood Cliffs, N.J., 1974.
12. D. M. YOUNG, "Iterative Methods for Solving Partial Difference Equations of Elliptic Type," Ph.D. Thesis, Harvard University, 1950.
13. R. S. VARGA, "Matrix Iterative Analysis," Prentice-Hall, Englewood Cliffs, N.J., 1962.
14. F. H. HARLOW AND A. A. AMSDEN, *J. Computational Phys.* **3** (1968), 80.
15. F. H. HARLOW AND A. A. AMSDEN, *J. Computational Phys.* **8** (1971), 197.
16. M. D. ROSEN, *Phys. Fluids* **18** (1975), 482.
17. S. C. JARDIN, *Phys. Fluids*, in press.